Joint effects of submesoscale lateral dispersion and biological reactions on biogeochemical flux

Lulabel R. Seitz[1], **Mara A. Freilich**[1,2]

[1]Division of Applied Mathematics, Brown University, Providence, RI 02912
[2]Department of Earth, Environmental, and Planetary Sciences, Brown University, Providence, RI 02912

Key Points:

- Increased dispersion, as an effect of lateral stirring, results in near-linear increases in phytoplankton flux.
- Lateral dispersion has the greatest impact on phytoplankton flux when the reactive timescale is small compared to the advective timescale.
- Flux is optimized at intermediate phytoplankton growth rates, another example of biophysical feedback that should be considered in modeling.

Corresponding author: Lulabel R. Seitz, lulabelseitz@gmail.com

Abstract

Submesoscale dynamics, operating at spatial scales of $\mathcal{O}(1-10$ km) and temporal scales of $\mathcal{O}(1$ day), are particularly important for marine ecosystems as they occur on similar timescales as phytoplankton growth, enabling biophysical feedbacks. While submesoscale dynamics are known to impact biological fluxes by modifying nutrient upwelling, horizontal transport has traditionally been assumed to only redistribute phytoplankton without altering concentrations. However, variations in submesoscale dispersion may significantly impact total biogeochemical flux if biological reactions occur during dispersal. By parameterizing the effects of dispersion due to lateral stirring on flux, within an eastern boundary current region, we show that enhanced dispersion yields a near-linear increase in offshore flux, with the magnitude modulated by phytoplankton growth rates and ambient nutrient availability. These findings identify a pathway for improving parameterizations of biogeochemical fluxes, while revealing a source of uncertainty in their prediction by climate models.

Plain Language Summary

Phytoplankton play a crucial role in Earth's climate by absorbing carbon dioxide from the atmosphere, making accurate predictions of their abundance essential for climate modeling. Ocean currents fundamentally shape phytoplankton communities by controlling their access to light and nutrients. However, computational limitations prevent climate models from representing ocean currents smaller than certain scales, such as the submesoscale, around 1-10 km. Dynamics occuring at the submesoscale operate on timescales similar to phytoplankton growth, paving the way for significant interactions between ocean movement and biological processes. Submesoscale dynamics are known to have a significant impact on phytoplankton growth by vertically transporting nutrients from deeper waters. These dynamics can also alter distributions of plankton and nutrients in the horizontal. Small-scale stirring motions can cause phytoplankton to scatter, or disperse, across the ocean surface. Using data from a coastal region, we find that dispersion leads to linear increases in the rate of transport of phytoplankton offshore, with the magnitude depending on both phytoplankton growth rates and ambient nutrient availability. Our findings suggest that climate models must account for how physical transport and biological responses of phytoplankton affect each other, and that ignoring these interactions may be a large source of uncertainty in predictions.

1 Introduction

Oceanic phytoplankton productivity is heterogeneous, with increased productivity in nutrient-rich areas, such as those near coastlines. Ocean currents redistribute plankton away from these productivity hotspots, providing crucial linkages between coastal and offshore regions. This transport is modulated by fine-scale ocean dynamics, which are unresolved in ocean general circulation models (OGCMs) and require parameterizations. To formulate accurate parameterizations, an understanding of the often complex biophysical feedbacks at these small scales is necessary, as eddy parameterizations of reactive tracers have been shown to perform poorly when they do not account for eddy reaction terms in addition to eddy flux terms (Prend et al., 2021).

Submesoscale dynamics, characterized by lateral scales of $\mathcal{O}$(1-10 km) and timescales of $\mathcal{O}(1$ day), and dynamically by $\mathcal{O}(1)$ Rossby and Richardson numbers, influence the abundance and distribution of phytoplankton through several mechanisms (McWilliams, 2016; Lévy et al., 2018; Lévy et al., 2023). These include nutrient transport into the euphotic zone due to enhanced vertical velocities, increased phytoplankton residence time in the euphotic layer due to reduced vertical mixing, and ecosystem restructuring caused by lateral stirring (Lévy et al., 2012; Mahadevan, 2016).

In this paper, we focus on the impact of submesoscale lateral dispersion on carbon flux in coastal regions. Lateral stirring has been shown to have a substantial impact on nutrient fluxes (Letscher et al., 2016) and plankton patchiness (Abraham, 1998; Mackas et al., 1985; Gangrade & Franks, 2023; Martin, 2003; Gower et al., 1980). The latter is significant because the contribution of phytoplankton to NPP is impacted by their spatial heterogeneity (Brentnall et al., 2003). The flux of biogeochemical tracers, rather than their distribution, is of particular interest as this quantity must be parameterized in OGCMs, and modelled tracer distributions have been found to be sensitive to the flux parameterization used (Fennel et al., 2022).

Unlike previous work that treated lateral stirring as a passive process, impacting only the distribution of phytoplankton and not their concentrations (Lévy et al., 2018), we use a coupled model to quantify the differential impact of lateral stirring based on biological factors. While the assumption that stirring is a passive process holds true when biological reactions are sufficiently slow, when the reaction timescales are large relative to the physical timescales, it is possible that there are considerable biophysical feedbacks. Since lateral stirring may have a stronger magnitude near surface, where phytoplankton are located, than in lower layers, where nutrients are stored and then upwelled, it is also not necessarily the case that nutrients and phytoplankton, which also have significant vertical gradients, are redistributed exactly together by lateral stirring. As a result, submesoscale modification of plankton dispersion can result in biophysical feedbacks.

We begin by discussing our modeling framework in §2. In §3, the results of computing biogeochemical fluxes along increasingly dispersive Lagrangian trajectories demonstrate that the impact of lateral dispersion on the flux indeed differs based on biological factors. Lastly, in §4, we discuss the implications for the uncertainty of NPP quantification, the enhancement of Lagrangian subgridscale models, and the improvement of parameterizations for biological transport.

2 Modeling Framework

Inspired by the approach of Freilich et al. (2022), we use an advection-reaction framework to compute the offshore phytoplankton biogeochemical flux along Lagrangian trajectories. As in that work, we explore the biological parameter space by varying the growth rate within the formulation of the phytoplankton growth (reaction) term. We explore the physical parameter space by using a Lagrangian subgridscale (LSGS) model, which parameterizes the effect of increasingly dispersive submesoscale dynamics on the flux. This representation of subgridscale effects is accomplished by modifying Lagrangian trajectories generated from coarse resolution velocity data according to target statistical measurements calculated from finer resolution, but more spatially limited, velocity data. In this analysis, we compute these statistics using surface drifter data, and simulate a range of values around the calculated values in order to determine the effect of varying the magnitude of dispersion. Then, to compute the flux, we formulate a reaction term based on a logistic population model, with an observation-informed carrying capacity.

The analysis is performed within an eastern boundary upwelling system, chosen for its surface drifter and biogeochemical data availability, which helps identify where the realistic scenario falls within the range of computed fluxes with varying dispersion.

2.1 Subgridscale Parameterization Scheme

Lagrangian stochastic (LS) models aim to represent particle motion within a turbulent flow by taking advantage of known statistics of the true velocity field (Thomson & Wilson, 2012). We use the Lagrangian subgridscale (LSGS) model proposed by Haza et al. (2007) and Haza et al. (2012), which is a deterministic model based on an LS model, to generate particle trajectories according to an increasingly dispersive "true" velocity

field. Unlike the more general LS models, the LSGS approach aims to *correct* the turbulent portion of model velocity fields only and generate trajectories according to that correction, to account for unresolved velocity components.

The LSGS model in two dimensions is formulated as follows. Given a lower-resolution observational velocity field $\mathbf{u}_m(t,x,y)$ (m subscript for "mesoscale"), a trajectory $\mathbf{x}_m : \mathbb{R} \to \mathbb{R}^2$ is formed by solving

$$\frac{d\mathbf{x}_m(t)}{dt} = \mathbf{u}_m(t,x,y). \tag{1}$$

We apply a Reynolds decomposition by taking a time-average,

$$\mathbf{u}_m(t,x,y) = \mathbf{U}_m(x,y) + \mathbf{u}'_m(t,x,y), \tag{2}$$

so that only the turbulent velocity $\mathbf{u}'_m$ is inaccurate due to the unresolved fine-scale dynamics. We approximate $\mathbf{U}_m(x,y)$ by a year-long time-average. The corrected trajectory $\mathbf{x}_c : \mathbb{R} \to \mathbb{R}^2$ is then found by solving

$$\frac{d\mathbf{x}_c}{dt} = \mathbf{U}_m(\mathbf{x}_c) + \mathbf{u}'_m(t,\mathbf{x}_c) + \boldsymbol{\eta}(t), \tag{3}$$

where $\boldsymbol{\eta}(t)$ is the correction found via the LSGS procedure. In particular, the zonal component of $\boldsymbol{\eta}(t) = (\eta^u(t), \eta^v(t))$ is found by solving

$$\frac{d\eta^u(t)}{dt} = a\frac{du'_m(t,\mathbf{x}_c(t))}{dt} + bu'_m(t,\mathbf{x}_c(t)) + c\eta^u(t). \tag{4}$$

The parameters in Eq. (4) are defined as

$$a = \left(\frac{\sigma_r^u}{\sqrt{\tau_r^u}}\right)\left(\frac{\sqrt{\tau_m^u}}{\sigma_m^u}\right) - 1, \quad b = \left(\frac{\sigma_r^u}{\sqrt{\tau_r^u}}\right)\left(\frac{\sigma_m^u}{\sqrt{\tau_m^u}}\right) - \frac{1}{\tau_r^u}, \text{ and } c = -\frac{1}{\tau_r^u}. \tag{5}$$

The meridional component $\eta^v(t)$ is found exactly analogously. The statistical parameters of interest – the turbulent velocity fluctuations (r.m.s. of turbulent velocity) $\boldsymbol{\sigma}$ and the decorrelation timescale $\boldsymbol{\tau}$ – appear in the parameters (5). Associated with the coarse velocity field $\mathbf{u}_m$ are $\boldsymbol{\sigma}_m = (\sigma_m^u, \sigma_m^v)$ and $\boldsymbol{\tau}_m = (\tau_m^u, \tau_m^v)$, where the superscript u denotes the zonal direction and the superscript v denotes the meridional direction. Similarly, there are statistics $\boldsymbol{\sigma}_r$ and $\boldsymbol{\tau}_r$ associated with the real velocity field.

In-situ position data from the Sub-Mesoscale Ocean Dynamics Experiment (S-MODE) field campaign are used to calculate σ_r and τ_r. The data are from 135 microstar surface drifters (1 m drogue), with observations at approximately five-minute intervals. All drifters were launched off the San Francisco coast in April 2023 (*S-MODE Mission Data*, 2024; Farrar et al., 2020).

Archiving, Validation and Interpretation of Satellite Oceanographic (AVISO) data are used for the low resolution velocity field $\mathbf{u}_m$. This coarser velocity field is geostrophic with Ekman surface currents, with a grid spacing of 0.25° by 0.25° and time intervals of six hours (Rio et al., 2014). The time range and domain of the AVISO data were chosen to match that of the drifter data. Trajectories are initialized using velocity data for April 11, 2023 at 00:00 UTC, and stepped forward until the last available time step on May 12, 2023 ($\sim 23:00$ UTC). One trajectory is initialized at each point in the 0.25° by 0.25° grid, within the region 140 W to 120 W longitude, 26 N to 42 N latitude, and trajectories that exit this region are not considered. The LSGS model involves a random initialization; we use an ensemble of 10 trajectories (see Supporting Information). The advective time-step is the time resolution of the AVISO data.

The LSGS model stems from the assumption that the trajectories can be described by a first-order LS model; in this context, the standard deviation of particle locations starting at the same initial point, in each direction, can be calculated as $\sqrt{2}\boldsymbol{\sigma}\sqrt{\boldsymbol{\tau}}$ (see SI). When using the LSGS model to generate trajectories corresponding to different amounts

of now-"resolved" subgridscale dispersion, by construction, $\boldsymbol{\sigma}_m$ and $\boldsymbol{\tau}_m$ remain constant. To simulate increasingly dispersive, hypothetical "true" scenarios, we vary $\boldsymbol{\sigma}_r\sqrt{\boldsymbol{\tau}_r}$, which we identify as the "dispersion parameter." Consequently, in generating trajectories, there are four parameters to vary: σ_r^u, σ_r^v, τ_r^u, and τ_r^v.

We modify trajectories computed using AVISO velocities via the LSGS methodology for a range of target values of the dispersion parameter; $\sigma_r^u, \sigma_r^v \in [0.05, 0.5]$ and $\tau_r^u, \tau_r^v \in [0.25, 1.075]$, all in increments of 0.025. These ranges were selected based on the submesoscale parameters calculated using the drifter data: $\sigma_r^u \approx 0.218$, $\sigma_r^v \approx 0.271$, $\tau_r^u \approx 0.772$, and $\tau_r^v \approx 0.698$. In order to distinguish the effect of varying the turbulent velocity fluctuations ($\boldsymbol{\sigma}_r$) versus that of varying the decorrelation timescale ($\boldsymbol{\tau}_r$), we only vary one in each simulation, while setting the other to be the calculated value from the drifter data.

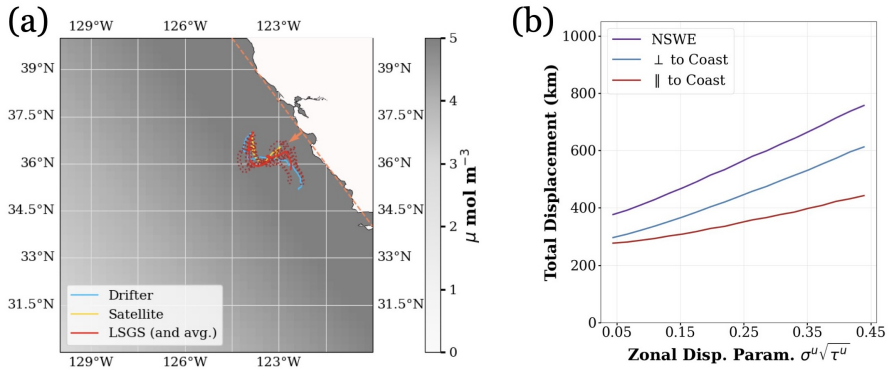

Figure 1. (a) A sample drifter trajectory (blue), a trajectory produced from the AVISO velocity field (yellow), and an LSGS trajectory (solid red), with the same initial condition, plotted over the realistic background nutrient gradient (shaded). The solid red line is produced from an average of the dotted red lines, which correspond to 10 random initializations of the LSGS procedure. The orange line approximates the coastline and the orange vector is unit normal. (b) The domain-averaged Euclidean displacement (purple), decomposed into displacements perpendicular (blue) and parallel (red) to the coast, plotted against the zonal dispersion parameter. Only σ^u is varied, since the zonal component is weighted more heavily in computing the offshore flux, while σ^v is fixed at 0.15.

The corrected velocity field associated with the produced trajectories has statistics closer to the target statistics computed over a submesoscale spatial domain, which has been referred to as "submesoscale dispersion" in this study. This is not intended to suggest that we only consider dispersion produced by $\mathcal{O}(1)$ Rossby and Richardson number features, as these dispersion statistics cannot be isolated from the smaller scale, *e.g. wave*, effects that also affect the drifter trajectories. Instead, the statistics are intended to represent the total effect of all dynamics that cause unresolved dispersion at the submesoscale.

2.2 Biological Model

In order to allow for nonlinear biological interactions while limiting the number of parameters, we represent the reaction term, *i.e.* the changes in phytoplankton concentration in response to nutrient availability, using a logistic model but with spatially-dependent

carrying capacity (c.f. Abraham, 1998). The system is given by

$$\frac{DP}{Dt} = \lambda P \left(1 - \frac{P}{N_0}\right), \tag{6}$$

where P is the concentration of phytoplankton (μmol m^{-3}), $D/Dt = \partial_t + \mathbf{v} \cdot \nabla$, and λ is a nutrient uptake rate parameter (s^{-1}).

The carrying capacity is set to be proportional to the spatially-dependent background nutrient gradient, $N_0 = N_0(x, y)$ (μmol m^{-3}). The initial condition P_0 is taken to be N_0. While Eq. (6) does not admit an analytical solution, it can be numerically approximated (see SI) and captures the observed heterogeneity of primary production. Although this simple representation of phytoplankton growth averages over more specific processes such as depletion due to grazing by zooplankton, nutrient limitation, remineralization, changes in community composition, etc., it importantly captures the nonlinearity of the growth while remaining conceptually tractable. In this work, we consider λ a constant parameter, but it can be a function of spatial, temporal, or other variables (Bonachela et al., 2011; Lomas et al., 2014).

The phytoplankton concentration anomaly is

$$P'(x, y, t) \equiv P(x, y, t) - P_0(x, y) = P(x, y, t) - N_0(x, y)$$

(with N_0 as before) and the velocity anomaly is

$$\mathbf{u}'(x, y, t) \equiv \mathbf{u}(x, y, t) - \mathbf{U}_m(x, y).$$

This identifies $\mathbf{U}_m(x, y) = \mathbf{U}_c(x, y)$, *i.e.*, the mean coarse resolution velocity field equals the mean "corrected" velocity field, which is consistent with the assumption that only the fluctuating portion of the coarse resolution velocity field should be modified by the LSGS procedure. The Lagrangian phytoplankton biogeochemical flux is then

$$\langle \mathbf{u}' P' \rangle_L, \tag{7}$$

where $\langle \cdot \rangle_L$ is the time average taken over the trajectory the flux is computed along, corresponding to the velocity $\mathbf{u}$. To obtain a scalar quantity, we consider the flux in the offshore direction, so each vector $\mathbf{u}'P'$ computed along a trajectory is dotted with a unit normal vector representing the offshore direction (Fig. 1a).

An average flux is then computed along each trajectory. Since the distribution of the average fluxes for each trajectory is approximately normal (Fig. 3, SI), a domain average is then taken of all the Lagrangian-averaged fluxes. In that manner, one final average flux value is obtained for each simulation. This is done for each of 20 logarithmically-spaced values of the uptake rate $\lambda \in [0.005 \text{ day}^{-1}, 2 \text{ day}^{-1}]$. Growth rates of 0.3-0.6 day^{-1} have been observed off the California coast (Landry et al., 2009).

2.3 Carrying Capacity

We formulate a realistic background (or time-mean) nutrient gradient based on nitrate data at the time and location of the drifter data, from the World Ocean Atlas (Reagan et al., 2024) (Fig. 1, SI). Although phytoplankton growth and survival is also dependent on light exposure and micronutrient concentration (Rhee & Gotham, 1981; Beardall et al., 2001; Glibert et al., 2016), we approximate the carrying capacity in relation to nitrate concentration (Dugdale et al., 2007). Since the carrying capacity is formulated in nitrogen units, phytoplankton concentration is as well.

Spatial variability in the carrying capacity or nutrient field has been invoked in prior studies (Abraham, 1998; Prend et al., 2021). Our application of this concept to a realistic scenario allows for synthesis of theoretical and observational results. Here, we make

use of the observed strong mean gradient of surface nutrient concentration within the California Current system (Legaard & Thomas 2006; Yu et al. 2021), as there is in many coastal environments. Although we expect that water parcels are dispersed horizontally with both plankton and nutrient together, these parcels are affected by vertical processes that result in a reduced carrying capacity on average in the offshore region. These processes include vertical nutrient supply, subduction, settling of cells and particles, and vertical migration by grazers. The carrying capacity is modeled such that this range of processes, which cannot be completely resolved, is still accounted for.

To better analyze how velocity fields versus background nutrient gradients affect flux, we run simulations with nutrient concentrations decaying linearly orthogonal to the coast, creating a primarily meridional gradient (Fig. 4, SI).

3 Results

The LSGS model successfully produces trajectories that are qualitatively more similar to the drifter trajectories than the uncorrected trajectories (Fig. 1a). The drifter trajectories have a higher calculated dispersion parameter ($\sigma_r^u\sqrt{\tau_r^u} \approx 0.191$, $\sigma_r^v\sqrt{\tau_r^v} \approx 0.226$) than the uncorrected trajectories ($\sigma_m^u\sqrt{\tau_m^u} \approx 0.159$, $\sigma_m^v\sqrt{\tau_m^v} \approx 0.211$). This motivates the question of whether particles following more dispersive trajectories have larger total displacements in general (*i.e.* the trajectories "wander around" more), which is the case when increasing the turbulent velocity fluctuations (Fig. 1). In this manner, a parcel carrying a community of phytoplankton that is subject to a more dispersive velocity field may meander more before going offshore, spending more time within the higher nutrient concentration (Fig. 1), eventually yielding higher offshore flux. From this, we may expect a (noisy) positive relationship between the dispersion parameter and the flux (Fig. 4-7, SI).

The average Lagrangian flux varies *nearly linearly* with the dispersion parameter, though the relationship is modulated by biological factors, including the direction of the carrying capacity gradient. Regardless of whether σ_r^u, σ_r^v, τ_r^u, or τ_r^v is varied, there is a positive, approximately linear relationship between the dispersion parameter and the average flux along trajectories (Fig. 2). The linearity of this relationship is unexpected given the nonlinear dependence of the flux $\langle \mathbf{u}'P' \rangle_L$ on these parameters, which affect both $\mathbf{u}'$, through the dependence of $\mathbf{x}_c$, Eq. (5), and P', through the dependence of N_0 on $\mathbf{x}_c$. The relationships differ slightly based on whether $\boldsymbol{\sigma}_r$ or $\boldsymbol{\tau}_r$ is varied, as expected due to the mathematical formulation Eq. (5).

The slope of the relationship between biogeochemical flux and the dispersion parameter depends nonlinearly on the biological uptake rate (Fig. 3). Since the velocity determines the location of the phytoplankton-laden parcel, and the concentration of phytoplankton is highly dependent on spatially-varying nutrient availability, P' may be considered a function of $\mathbf{u}'$. Thus, modifications to the velocity field can affect the flux nonlinearly via biological factors. In particular, the uptake rate that maximizes the average flux for any value of the dispersion parameter, in all cases, is an intermediate one among the simulated range. Freilich et al. (2022) found a similar result, that intermediate growth rates maximize phytoplankton flux vertically. Fig. 4 shows that submesoscale lateral dispersion can have a differential impact on the phytoplankton biogeochemical flux depending on the growth rate.

Although lateral dispersion significantly affects the magnitude of the flux, our results do not provide evidence that it can reverse the direction (or sign) of the flux, when considering a realistic background nutrient gradient. As expected, due to the eastern boundary, the average flux is westward in each case. Note that while Fig. 3 shows some small negative intercepts for the best fit lines, the LSGS procedure did not produce negative fluxes.

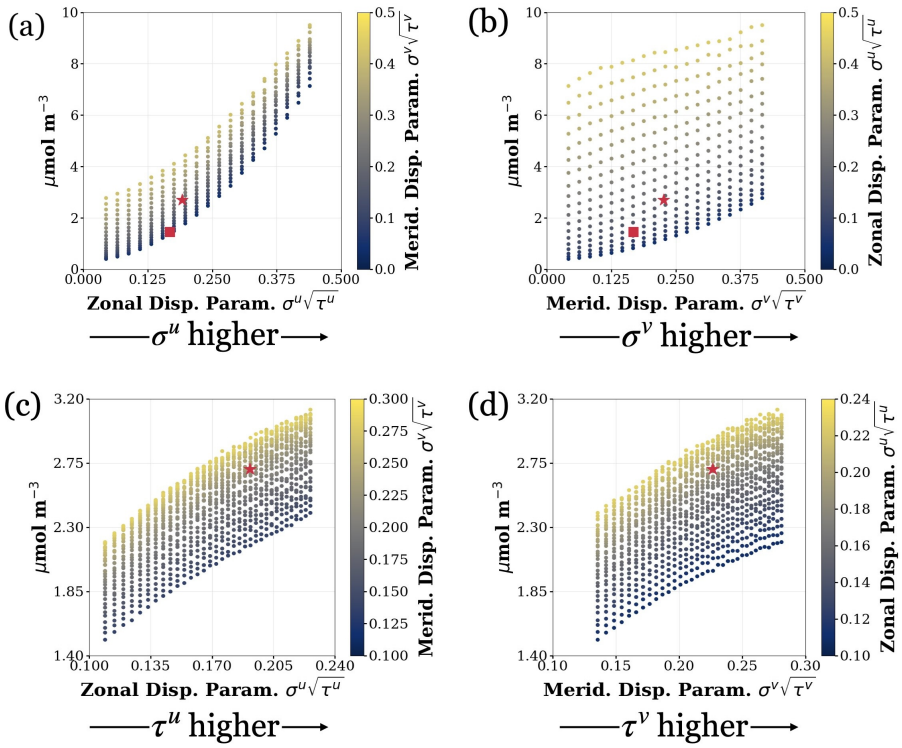

Figure 2. Domain-averaged Lagrangian flux $\langle \mathbf{u}'P' \rangle_L$ versus the dispersion parameter in one direction, with fixed uptake rate $\lambda = 1.0645$ day^{-1}. Points are colored by the dispersion parameter in the direction not plotted on the x-axis. Top: dispersion is modified by varying the turbulent velocity fluctuations $\boldsymbol{\sigma}_r$, (a) zonally and (b) meridionally. The red stars show the flux corresponding to the drifter dispersion parameter value, while the red squares show that calculated from the uncorrected/AVISO-only simulation. Bottom: dispersion is modified by varying the decorrelation timescale $\boldsymbol{\tau}_r$, (c) zonally and (d) meridionally. The flux for the uncorrected simulation is not shown, as simulating that value of the dispersion parameter would require very unrealistic values of τ_r^u, τ_r^v.

The direction of stronger mean velocity, which is aligned with a strong tracer gradient in physically realistic scenarios, should have a greater impact on flux. This is reflected in the relative tightness of the linear relationship in Fig. 2a,c compared to b,d. Comparison to the simulations with reversed background nutrient gradient shows that the relative impact of zonal versus meridional dispersion depends on the direction of the background nutrient gradient, underscoring the significance of the relationship between the mean flow and the resource landscape. Varying the dispersion parameter has a greater impact on the average flux when the direction of the gradient and the flux are aligned (Fig. 4, SI). The interplay between the distribution of resources, which is spatially heterogeneous, and dispersion, which is strongly impacted by fine-scale dynamics, is thus another mechanism through which physical and biological dynamics are coupled.

With any amount of dispersion, the flux is a nonlinear function of the uptake rate, with two key characteristics. First, for a given dispersion parameter, the flux is maximized at an intermediate value of the uptake rate ($\approx 10^{-1}$, Fig. 4). Although the relationships in Fig. 4 depend on the velocity field and cannot be predicted *a priori*, they follow the pattern that the flux monotonically increases until it is maximized at an in-

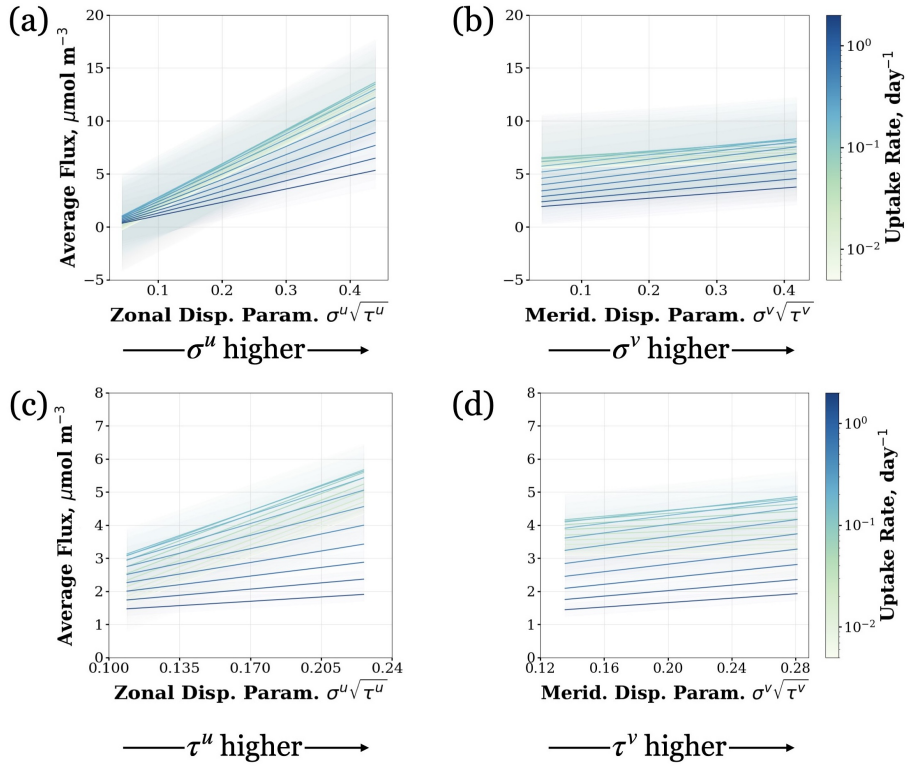

Figure 3. The dependence of the flux on the dispersion is mediated by the uptake rate. The best fit corresponding to the scatter plots, as in Fig. 2, for 20 uptake rates. Line colors indicate uptake rate, with shading showing standard deviation. Top: effect of varying the turbulent velocity fluctuations $\boldsymbol{\sigma}_r$, (a) zonally and (b) meridionally. Bottom: same as the top, but varying the decorrelation timescale $\boldsymbol{\tau}_r$, (c) zonally and (d) meridionally.

termediate value of the uptake rate and decreases thereafter, which could be predicted from the formulation of the reaction term. Too low of an uptake rate will cause the concentration to always stay well below carrying capacity, while too high of an uptake rate will cause the concentration to exceed it, causing it to then decrease. The preference for an intermediate uptake rate reflects that a balance between nutrient uptake and resupply is optimal for growth.

Second, for smaller and suboptimal growth rates, the phytoplankton flux is more strongly influenced by lateral stirring. In Fig. 4c,d, varying the decorrelation timescale ($\boldsymbol{\tau}_r$), which may be considered the advective timescale, has more of an effect on the average flux in the regime in which the uptake rate is lower. The shape of the trends in Fig. 4c,d generally reflects that transport is optimized when the timescales of reactions and advection are of approximately the same order (Freilich et al., 2022). By simultaneously varying the biological and physical parameters, two distinct effects are revealed: universal maximization of flux at an intermediate uptake rate and increased sensitivity of flux to lateral stirring when the reaction timescale is faster than the advective timescale.

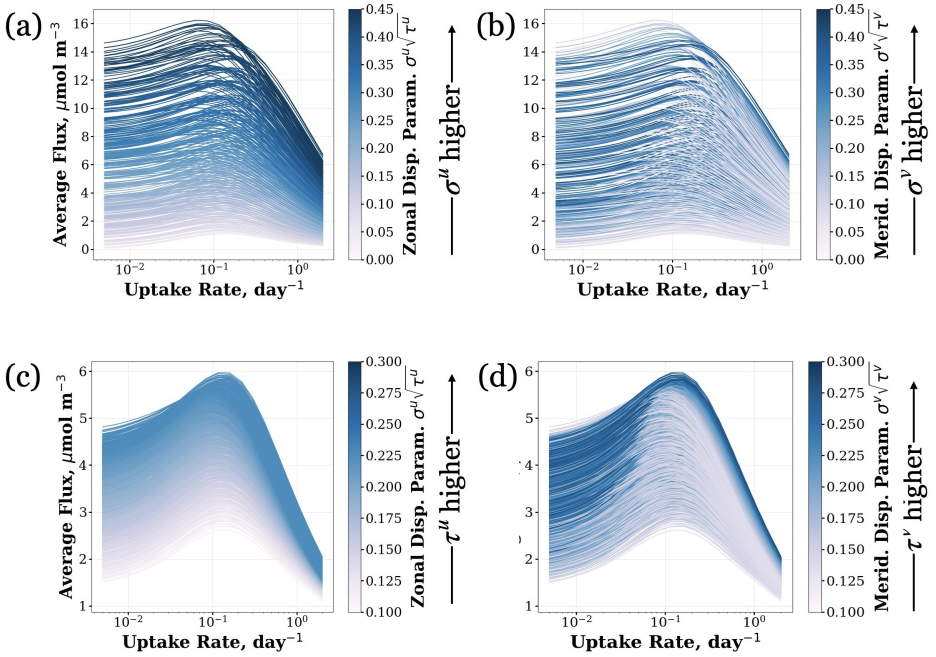

Figure 4. Average flux across Lagrangian trajectories versus the uptake rate λ, for different amounts of dispersion. Top: dispersion increased by increasing the turbulent velocity fluctuations $\boldsymbol{\sigma}_r$, (a) zonally and (b) meridionally. Bottom: dispersion increased by increasing the decorrelation timescale $\boldsymbol{\tau}_r$, (c) zonally and (d) meridionally.

4 Discussion and Conclusion

In this study, we explore both the physical and biological parameter spaces to analyze the coupled impact of submesoscale lateral dispersion and nonlinear biological reactions on offshore phytoplankton biogeochemical flux. We find in each case that there is a near-linear relationship between the average, lateral Lagrangian flux and the dispersion parameter. Moreover, we find that the impact of the dispersion parameter on the average flux depends on both the biological uptake rate and the background nutrient gradient. In any case, the results indicate that increased resolved lateral dispersion corresponds to increased calculated offshore flux.

These insights are particularly relevant in the context of the well-established uncertainty of predictions of the response of biological carbon transport to the changing climate (Brett et al., 2021; Henson et al., 2022). Given that the calculated dispersion parameter values for the AVISO data were much smaller than those for the drifter data, the inability to accurately gauge the effect of unresolved subgridscale dispersion on biological carbon flux may be another major contributor to this prediction uncertainty. This is especially true given that dispersion is likely underrepresented in ocean models (Schroeder et al., 2012). Trajectories derived from both models and altimetry observations have poor agreement with submesoscale observational data in other regions as well. In general, drifter observations show faster dispersion than modeled or satellite altimetry derived velocity fields (Poje et al., 2014).

The lateral redistribution of nutrients, particularly in regions with strong gradients, has a significant impact on the magnitude of primary production, export production, and availability of nutrients (Stukel & Barbeau, 2020). Thus, the discrepancy be-

tween the calculated flux for the trajectories generated with the submesoscale drifter dispersion parameter versus that for the uncorrected trajectories (Fig. 2a,b) emphasizes the importance of accounting for subgridscale dispersion in both models and observations to accurately estimate climatological impacts on the NPP.

One of the major limitations of many satellite NPP algorithms is that they do not account for the Lagrangian nature of ocean ecosystems (Kuhn et al., 2023). They instead assume that production occurs where plankton are found. More recent work overcomes this limitation, but is constrained by the lack of availability of submesoscale velocity fields (Jönsson & Salisbury, 2016; Messié et al., 2022). The methodology developed in this paper can be used to contextualize – or even directly employed to analyze – how subgridscale dispersion may influence the results obtained by these algorithms.

In the context of the LSGS model used, which lacks a mechanism for energized smaller scales to influence dispersion, the long-time effects of decreasing the decorrelation timescale may be inaccurately represented. This is a by-product of the assumption that $\boldsymbol{\sigma}_r$ and $\boldsymbol{\tau}_r$ are constant in time (Haza et al., 2007). Although it is beyond the scope of this work to propose an enhanced LSGS model, LSGS models may be improved by considering statistics at multiple scales or otherwise allowing a bidirectional energy cascade. The submesoscale is characterized by both upscale and downscale energy fluxes (McWilliams, 2016); future work should analyze the impact of this characteristic on biogeochemical fluxes. Nevertheless, the decorrelation timescale produces a coherent trend in relation to the flux – especially τ_r^u, not unexpectedly since the flux direction is primarily zonal – in a manner that seemingly depends on the biological timescale. As a result, this statistic may be a useful ingredient for parameterizations in this biological context. Developing parameterizations that account for the interaction between the biological timescale λ and physical timescale τ (Fig. 4) is worthy of further investigation.

Our results suggest that interactions between submesoscale lateral dispersion and biological reactions are an important factor to consider when formulating parameterizations, building upon previous findings that in the case of vertical flux, parameterizations must account for biophysical coupling (Freilich et al., 2022) and that when parameterizing biogeochemical flux, the impact of nonlinear reactions must be handled carefully (Prend et al., 2021). The lateral stirring of biogeochemical tracers cannot be accurately modeled as a perfectly passive process. This further motivates the development of more biologically informed parameterizations and those that account for non-local effects.

Open Research Section

The code to complete all aspects of the simulations and analysis is available at `https://github.com/freilich-lab/submesoscale-lsgs` and archived at 10.5281/zenodo.14278765. The drifter data used were all of the 2023 trajectories from S-MODE: `https://catalog.data.gov/dataset/s-mode-l2-position-data-from-surface-drifters-version-1`. The AVISO data used can be downloaded from `https://data.marine.copernicus.eu/product/MULTIOBS_GLO_PHY_MYNRT_015_003/services`.

Acknowledgments

The authors acknowledge support from NASA grants 80NSSC24K1422 and 80NSSC24K0410. LRS was supported by the National Defense Science and Engineering Graduate (NDSEG) Fellowship, sponsored by the U.S. Department of Defense. The authors are grateful to the Sub-Mesoscale Ocean Dynamics Experiment science team and the captain and crew of the R/V Sally Ride. The authors appreciate comments from Baylor Fox-Kemper, Lilian Dove, and Élise Beaudin.

References

Abraham, E. R. (1998, February). The generation of plankton patchiness by turbulent stirring. *Nature*, *391*(6667), 577–580.

Beardall, J., Young, E., & Roberts, S. (2001). Approaches for determining phytoplankton nutrient limitation. *Aquatic sciences*, *63*, 44–69.

Bonachela, J. A., Raghib, M., & Levin, S. A. (2011, December). Dynamic model of flexible phytoplankton nutrient uptake. *Proc. Natl. Acad. Sci. U. S. A.*, *108*(51), 20633–20638.

Brentnall, S. J., Richards, K. J., Brindley, J., & Murphy, E. (2003, February). Plankton patchiness and its effect on larger-scale productivity. *J. Plankton Res.*, *25*(2), 121–140.

Brett, G. J., Whitt, D. B., Long, M. C., Bryan, F., Feloy, K., & Richards, K. J. (2021, May). Sensitivity of 21st-century projected ocean new production changes to idealized biogeochemical model structure. *Biogeosciences*, *18*(10), 3123–3145.

Dugdale, R. C., Wilkerson, F. P., Hogue, V. E., & Marchi, A. (2007, June). The role of ammonium and nitrate in spring bloom development in san francisco bay. *Estuar. Coast. Shelf Sci.*, *73*(1-2), 17–29.

Farrar, J. T., D'Asaro, E., Rodriguez, E., Shcherbina, A., Czech, E., Matthias, P., ... others (2020). S-MODE: The sub-mesoscale ocean dynamics experiment. In *Igarss 2020-2020 ieee international geoscience and remote sensing symposium* (pp. 3533–3536).

Fennel, K., Mattern, J. P., Doney, S. C., Bopp, L., Moore, A. M., Wang, B., & Yu, L. (2022). Ocean biogeochemical modelling. *Nature Reviews Methods Primers*, *2*(1), 76.

Freilich, M. A., Flierl, G., & Mahadevan, A. (2022, February). Diversity of growth rates maximizes phytoplankton productivity in an eddying ocean. *Geophys. Res. Lett.*, *49*(3).

Gangrade, S., & Franks, P. J. S. (2023, March). Phytoplankton patches at oceanic fronts are linked to coastal upwelling pulses: Observations and implications in the California Current System. *J. Geophys. Res. C: Oceans*, *128*(3).

Glibert, P. M., Wilkerson, F. P., Dugdale, R. C., Raven, J. A., Dupont, C. L., Leavitt, P. R., ... Kana, T. M. (2016). Pluses and minuses of ammonium and nitrate uptake and assimilation by phytoplankton and implications for productivity and community composition, with emphasis on nitrogen-enriched conditions. *Limnology and Oceanography*, *61*(1), 165–197.

Gower, J. F. R., Denman, K. L., & Holyer, R. J. (1980, November). Phytoplankton patchiness indicates the fluctuation spectrum of mesoscale oceanic structure. *Nature*, *288*(5787), 157–159.

Haza, A. C., Piterbarg, L. I., Martin, P., Özgökmen, T. M., & Griffa, A. (2007). A Lagrangian subgridscale model for particle transport improvement and application in the Adriatic Sea using the Navy Coastal Ocean Model. *Ocean Modelling*, *17*(1), 68-91.

Haza, A. C., Özgökmen, T. M., Griffa, A., Garraffo, Z. D., & Piterbarg, L. (2012, January). Parameterization of particle transport at submesoscales in the Gulf Stream region using Lagrangian subgridscale models. *Ocean Model.*, *42*, 31–49.

Henson, S. A., Laufkötter, C., Leung, S., Giering, S. L. C., Palevsky, H. I., & Cavan, E. L. (2022, April). Uncertain response of ocean biological carbon export in a changing world. *Nat. Geosci.*, *15*(4), 248–254.

Jönsson, B. F., & Salisbury, J. E. (2016). Episodicity in phytoplankton dynamics in a coastal region. *Geophysical Research Letters*, *43*(11), 5821–5828.

Kuhn, A. M., Mazloff, M., Dutkiewicz, S., Jahn, O., Clayton, S., Rynearson, T., & Barton, A. D. (2023). A global comparison of marine chlorophyll variability observed in Eulerian and Lagrangian perspectives. *Journal of Geophysical Research:*

Oceans, *128*(7), e2023JC019801.

Landry, M. R., Ohman, M. D., Goericke, R., Stukel, M. R., & Tsyrklevich, K. (2009, December). Lagrangian studies of phytoplankton growth and grazing relationships in a coastal upwelling ecosystem off Southern California. *Prog. Oceanogr.*, *83*(1-4), 208–216.

Legaard, K. R., & Thomas, A. C. (2006). Spatial patterns in seasonal and interannual variability of chlorophyll and sea surface temperature in the California Current. *Journal of Geophysical Research: Oceans*, *111*(C6).

Letscher, R. T., Primeau, F., & Moore, J. K. (2016, October). Nutrient budgets in the subtropical ocean gyres dominated by lateral transport. *Nat. Geosci.*, *9*(11), 815–819.

Lévy, M., Couespel, D., Haëck, C., Keerthi, M. G., Mangolte, I., & Prend, C. J. (2023, June). The impact of fine-scale currents on biogeochemical cycles in a changing ocean. *Ann. Rev. Mar. Sci.*.

Lévy, M., Ferrari, R., Franks, P. J., Martin, A. P., & Rivière, P. (2012). Bringing physics to life at the submesoscale. *Geophysical Research Letters*, *39*(14).

Lévy, M., Franks, P. J., & Smith, K. S. (2018). The role of submesoscale currents in structuring marine ecosystems. *Nature communications*, *9*(1), 4758.

Lomas, M. W., Bonachela, J. A., Levin, S. A., & Martiny, A. C. (2014, December). Impact of ocean phytoplankton diversity on phosphate uptake. *Proc. Natl. Acad. Sci. U. S. A.*, *111*(49), 17540–17545.

Mackas, D. L., Denman, K. L., & Abbott, M. R. (1985). Plankton patchiness: biology in the physical vernacular. *Bull. Mar. Sci.*, *37*(2), 652–674.

Mahadevan, A. (2016). The impact of submesoscale physics on primary productivity of plankton. *Annual review of marine science*, *8*, 161–184.

Martin, A. P. (2003, May). Phytoplankton patchiness: the role of lateral stirring and mixing. *Prog. Oceanogr.*, *57*(2), 125–174.

McWilliams, J. C. (2016, May). Submesoscale currents in the ocean. *Proc. Math. Phys. Eng. Sci.*, *472*(2189), 20160117.

Messié, M., Sancho-Gallegos, D. A., Fiechter, J., Santora, J. A., & Chavez, F. P. (2022, May). Satellite-based Lagrangian model reveals how upwelling and oceanic circulation shape krill hotspots in the California Current System. *Front. Mar. Sci.*, *9*, 835813.

Poje, A. C., Ozgökmen, T. M., Lipphardt, B. L., Jr, Haus, B. K., Ryan, E. H., Haza, A. C., ... Mariano, A. J. (2014, September). Submesoscale dispersion in the vicinity of the Deepwater Horizon spill. *Proc. Natl. Acad. Sci. U. S. A.*, *111*(35), 12693–12698.

Prend, C. J., Flierl, G. R., Smith, K. M., & Kaminski, A. K. (2021). Parameterizing eddy transport of biogeochemical tracers. *Geophysical Research Letters*, *48*(21), e2021GL094405.

Reagan, J. R., Boyer, T. P., García, H. E., Locarnini, R. A., Baranova, O. K., Bouchard, C., ... Dukhovskoy, D. (2024). *World Ocean Atlas 2023.* NOAA National Centers for Environmental Information. (Dataset: NCEI Accession 0270533)

Rhee, G.-Y., & Gotham, I. J. (1981). The effect of environmental factors on phytoplankton growth: light and the interactions of light with nitrate limitation 1. *Limnology and Oceanography*, *26*(4), 649–659.

Rio, M.-H., Mulet, S., & Picot, N. (2014). Beyond GOCE for the ocean circulation estimate: Synergetic use of altimetry, gravimetry, and in situ data provides new insight into geostrophic and Ekman currents. *Geophysical Research Letters*, *41*(24), 8918-8925.

Schroeder, K., Chiggiato, J., Haza, A. C., Griffa, A., Özgökmen, T. M., Zanasca, P., ... Trees, C. (2012, June). Targeted Lagrangian sampling of submesoscale dispersion at a coastal frontal zone. *Geophysical Research Letters*, *39*(11).

S-MODE mission data. (2024). Retrieved from `https://podaac.jpl.nasa.gov/s-mode?tab=mission-objectives&sections=about%2Bdata` (PO.DAAC, CA, USA. Dataset accessed 2024-06-03)

Stukel, M. R., & Barbeau, K. (2020). Investigating the nutrient landscape in a coastal upwelling region and its relationship to the biological carbon pump. *Geophysical Research Letters*, *47*(6), e2020GL087351.

Thomson, D., & Wilson, J. (2012, 01). History of Lagrangian stochastic models for turbulent dispersion. In (Vol. 200, p. 19-36). doi: 10.1029/2012GM001238

Yu, X., Chen, S., & Chai, F. (2021). Remote estimation of sea surface nitrate in the California current system from satellite ocean color measurements. *IEEE Transactions on Geoscience and Remote Sensing*, *60*, 1–17.

Geophysical Research Letters

Supporting Information for

"Joint effects of submesoscale lateral dispersion and biological reactions on biogeochemical flux"

Lulabel R. Seitz[1], Mara A. Freilich[1,2]

[1] Division of Applied Mathematics, Brown University, Providence, RI 02912 [2]Department of Earth, Environmental, and Planetary Sciences, Brown University, Providence, RI 02912

Contents of this file

Text S1. Theoretical Framework for LSGS Model and Dispersion Parameter

Although the full details of the derivation of the LSGS model can be found in Haza et al. (2007), we give an overview here. The first assumption is that the trajectories produced by the "true" velocity field and coarse resolution (or model) velocity field follow a first-order Markov model. For the real/true velocity field, whose associated quantities are denoted with a subscript r, we assume

$$\begin{aligned} \mathrm{d}\mathbf{x}_r &= (\mathbf{u}_r(t,\mathbf{x}_r) + \mathbf{u}_r')\mathrm{d}t \\ \mathrm{d}\mathbf{u}_r' &= \Lambda_r \mathrm{d}\boldsymbol{\xi} - A_r \mathbf{u}_r' \mathrm{d}t \end{aligned} \tag{1}$$

so that $\mathbf{u}_r(t,\mathbf{x}_r(t))$ is the deterministic drift, $\boldsymbol{\xi}$ denotes a two-dimensional Wiener process, $\mathbf{u}_r'$ is a fluctuation velocity with zero mean, A_r is the dissipation matrix, and Λ_r is the dispersion matrix. Exactly analogous equations can be written for the coarse resolution velocity fields, denoted with a subscript m. In the case of zero spin, the dissipation and dispersion matrices are defined by

$$A_r = \begin{bmatrix} \frac{1}{\tau_r^u} & 0 \\ 0 & \frac{1}{\tau_r^v} \end{bmatrix} \quad \text{and} \quad \Lambda_r = \begin{bmatrix} \sigma_r^u \sqrt{\frac{2}{\tau_r^u}} & 0 \\ 0 & \sigma_r^v \sqrt{\frac{2}{\tau_r^v}} \end{bmatrix}.$$

These matrices but for the coarse velocity field, A_m and Λ_m, are defined exactly analogously. The difference between these matrices – A_r versus A_m and Λ_r versus Λ_m – depends only on $\boldsymbol{\sigma}_r$, $\boldsymbol{\sigma}_m$, $\boldsymbol{\tau}_r$, and $\boldsymbol{\tau}_m$, and is what is used to formulate the LSGS model proposed by Haza et al. (2007). With the assumption that both velocity fields produce trajectories governed by the above stochastic differential equations, we aim to find a random vector process, which can be considered the subgridscale component, $\boldsymbol{\eta}(t)$, in order to formulate corrected trajectory positions $\mathbf{x}_c(t)$ such that it and the associated velocity field,

$$\mathbf{u}_c(t) \doteq \mathbf{u}_m(t) + \boldsymbol{\eta}(t)$$

have the same pdf $p(t, \mathbf{u}_c, \mathbf{x}_c)$ as a real particle given the same initial condition, for all relevant times t. The authors then argue that finding $\boldsymbol{\eta} = (\eta^u, \eta^v)$ according to the equation

$$\frac{d\eta^u}{dt} = a\frac{du'_m}{dt} + bu'_m + c\eta^u$$

where

$$a \doteq \frac{\sigma_r^u\sqrt{\tau_m^u}}{\sigma_m^u\sqrt{\tau_u^r}} - 1, \quad b \doteq \frac{\sigma_r^u}{\sigma_m^u\sqrt{\tau_r^u\tau_m^u}} - \frac{1}{\tau_r}, \quad c \doteq -\frac{1}{\tau_r^u}$$

with a specific random initialization, corresponds to a stationary solution of $\boldsymbol{\eta}$ that yields "statistically equivalent" corrected and real velocity fields. Notice the above is not an SDE, but an ODE, and that we have arrived at a *deterministic* (except for the initial condition), rather than stochastic, model. The random initialization is that $\eta^u(0)$ should be drawn from a normal distribution with mean zero and variance

$$\overline{(\eta^u)^2} = \frac{(\sigma_r^u/\sqrt{\tau_m^u} - \sigma_m^u/\sqrt{\tau_r^u})^2 + (\sigma_r^u\sqrt{\tau_r^u} - \sigma_m^u\sqrt{\tau_m^u})^2}{\tau_r^u + \tau_m^u},$$

and analogously for η^v. From this, the authors propose a spatially-dependent version of the above equations, which we used for our analysis. Despite the limitations associated with the assumptions made in this derivation, this LSGS model showed good performance in creating corrected trajectories with approximately the target statistics (Haza et al., 2007). This is clearly advantageous when compared to more general Lagrangian stochastic models when one has observational or fine resolution velocity data, as it can take advantage of this available statistical information. It is also advantageous for the scenario in which one specifically wants to assess the affect of varying the target parameters. Additionally, since the final form of the model is deterministic, it has a much lower computational cost than using a truly stochastic model.

By calculating the standard deviation of the locations of particle trajectories, we can see how the dispersion parameter $\sigma\sqrt{\tau}$ arises naturally. As in Pope (2001), we consider dispersion from a point source in statistically stationary isotropic turbulence. Suppose the unit source is at the origin and the release of the particles is at $t = 0$. Since we are considering multiple particles from the same source, we emphasize that σ is the r.m.s. velocity (the square root of the arithmetic mean of the variances of the turbulence velocity corresponding to each particle). We also define $\rho(s)$ to be the Lagrangian velocity autocorrelation function. Then we can calculate the covariance of the fluid particle position to be

$$\begin{aligned}\langle \boldsymbol{x}_i(t)\boldsymbol{x}_j(t)\rangle &= \int_0^t\int_0^t \langle \boldsymbol{u}_i(t')\boldsymbol{u}_j(t'')\rangle dt'dt'' \\ &= \int_0^t\int_0^t \sigma^2\rho(t'-t'')\delta_{ij}dt'dt''.\end{aligned}$$

The covariance of position is also isotropic so

$$\langle \boldsymbol{x}_i(t)\boldsymbol{x}_j(t)\rangle = \sigma_X^2(t)\delta_{ij},$$

where $\sigma_X(t)$ denotes the standard deviation for the particle positions, which is the dispersion from the point source. Then

$$\begin{aligned}\sigma_X^2(t) &= \sigma^2\int_0^t\int_0^t \rho(t'-t'')\delta_{ij}dt'dt'' \\ &= 2\sigma^2\int_0^t (t-s)\rho(s)ds.\end{aligned}$$

We are interested in the regime where $t \gg \tau$, since we are interested in the dispersion for trajectories integrated forward for a month while the calculated decorrelation timescales are on the order of a day. In this long-time regime, we approximate

$$\int_0^t (t-s)\rho(s)ds \approx t\int_0^\infty \rho(s)ds = t\tau$$

(note that the τ we use in practice is an approximation of this τ). Then we see that

$$\sigma_X(t) \approx \sqrt{2}\sigma\sqrt{\tau t}.$$

Since in all simulations we integrate trajectories for the same amount of time, we can increase the expected dispersion of the trajectories by increasing $\sigma\sqrt{\tau}$, which we defined to be the dispersion parameter. This also relates to a simple approximation of the eddy diffusivity coefficient; this dispersion can also be thought of as diffusion with constant diffusivity $\sigma^2\tau$.

In the random flight model Eq. (1), the scaling on the random forcing appears, up to constant, as the entries of the dispersion matrix Λ. This matrix has been referred to as the “dispersion matrix" not only in Haza et al. (2007) but also prior work, seemingly stemming back to Raupach (1989). From an intuitive standpoint, this could be identified as the “dispersion parameter" because the random forcing is what should cause more dispersion in the generated trajectories, by modifying the fluctuation velocity, larger values of the scaling coefficient should yield more dispersion. The physical meaning of $\boldsymbol{\sigma}$ and $\boldsymbol{\tau}$ could also be used to justify this alternative definition of the dispersion parameter; decreasing the decorrelation timescale could be thought to lead to more dispersion, since a less correlated velocity field allows particles to experience more variability in both the direction and magnitude of their velocities. It should also be noted that the LSGS model is somewhat of a “steady-state" approximation to (1), so the role of each component of the dispersion parameter is not necessarily the same. Yet, we empirically find that decreasing τ does not actually increase dispersion, which is further justification for defining the dispersion parameter as in the main text. The domain averages of the Lagrangian-averaged velocity variance for different trials with increasing values of the dispersion parameter, which were increased by decreasing $\boldsymbol{\tau}$ while holding $\boldsymbol{\sigma}$ fixed, is shown in Figure S1.

Text S2. Additional Details for Biological Model

Approximation to WOA Data and Units. The first iteration of the background nutrient gradient was formulated to approximately match real values of nitrate concentrations from World Ocean Atlas data. The WOA data showed a very similar near-linear decay, and the approximation was with an exactly linear decay. We approximated the coastline over the domain of interest with the line going through the points $(-124.5, 40)$ and $(-120, 34)$. The normal vector to the coastline was taken by normalizing the vector $[m, -1]^T$ where m is the slope of the approximate coastline. The background nutrient concentration at a given point was then calculated based on the distance to the coastline, with a maximum value set at 5.5 and a decay rate of 0.25 with distance from the coastline. Given the coarse time and space resolution of the WOA data, these choices were made somewhat arbitrarily, just to approximately match the WOA data while maintaining linearity (for ease of calculation when computing the flux) and that all concentration values within the domain are positive. The nutrient values were converted from μmol kg^{-1} to μmol m^{-3} by multiplying by 1025 kg m^{-3}.

The reversed nutrient gradient was constructed in the same way as the realistic background nutrient gradient. Instead of calculating the distance from the coast though, a line perpendicular to the coast was approximated. The gradient was then formed with a maximum of 5.5 and a decay rate of 0.3.

Throughout, the phytoplankton flux is considered in nitrogen units. However, this is directly proportional to phytoplankton carbon flux, for instance, by employing a conversion according to the Redfield

ratio.

Lack of Analytical Solution. To solve for P', we just (numerically) solve for P at each trajectory point and then subtract P_0 (which does not evolve in time, so has a determined value at the given trajectory point), since we assume $P = P' + P_0$.

If we had a constant carrying capacity K, we could solve the equation for P via the method of characteristics to obtain the solution

$$P(x, y, t) = \frac{Kf(s, r)}{\frac{1}{K}e^{-\lambda t} + (1 - e^{-\lambda t})f(s, r)} \tag{2}$$

where f is the initial condition for P, and s is the initial condition for the ODE

$$\frac{dx(t)}{dt} = u(x, y, t)$$

while r is the initial condition for the ODE

$$\frac{dy(t)}{dt} = v(x, y, t).$$

Given explicit velocity fields in each direction over the time interval, $u(x, y, t)$ and $v(x, y, t)$, we can then find an exact solution for the concentration. However, if we instead consider a spatially-varying carrying capacity so that the system is

$$\frac{\partial P}{\partial t} + \boldsymbol{u}\frac{\partial P}{\partial \boldsymbol{x}} = \lambda P\left(1 - \frac{P}{K(\boldsymbol{x})}\right).$$

Using the method of characteristics, we have

$$\frac{dt}{ds} = 1, \quad \frac{dx}{ds} = \boldsymbol{u}(\boldsymbol{x}, t), \quad \frac{dP}{ds} = \lambda P\left(1 - \frac{P}{K(\boldsymbol{x})}\right).$$

At this point, we can see that an analytical solution is not possible because the $\frac{dP}{ds}$ equation is not separable, since we cannot factor out the $\boldsymbol{x}(s)$ term. To our knowledge, there is no other method to obtain an analytical solution for this equation, especially given that we do not have a closed-form expression for our velocity field. However, the ODE is simple enough that it can be numerically approximated; we use a Runge-Kutta scheme (RK45 in SciPy).

References From the Supporting Information

Raupach, M. R. (1989). Applying Lagrangian fluid mechanics to infer scalar source distributions from concentration profiles in plant canopies. Agricultural and Forest Meteorology, 47(2-4), 85-108.

Pope, S. B. (2001). Turbulent flows. Measurement Science and Technology, 12(11), 2020-2021.

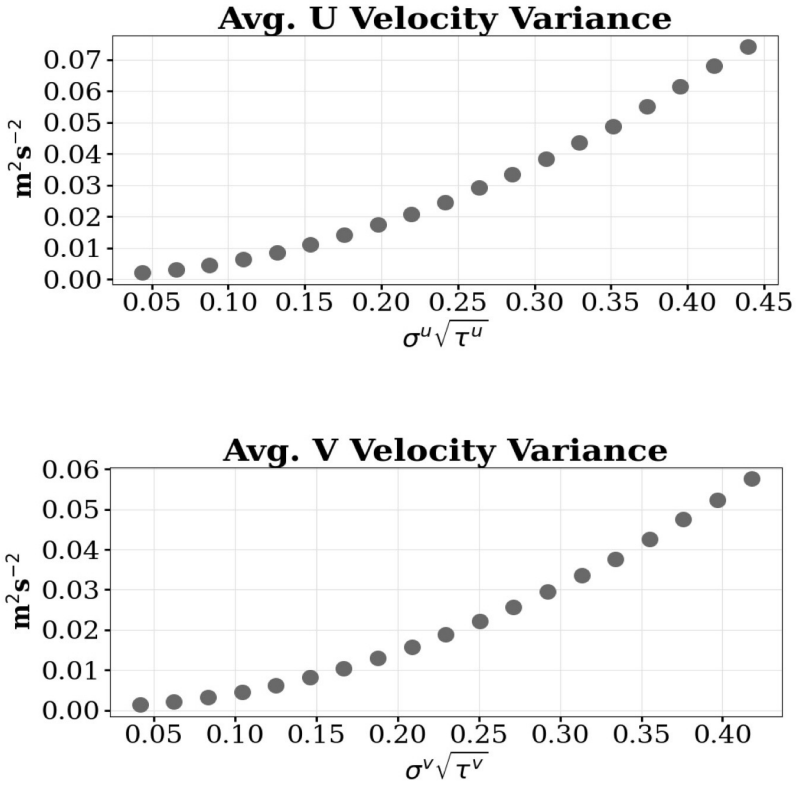

Figure S1: The average velocity variance holding $\boldsymbol{\sigma}$ fixed but varying $\boldsymbol{\tau}$. The top figure shows the average zonal velocity variance vs. the dispersion parameter, where $\boldsymbol{\sigma}$ is held fixed at the drifter parameters and τ^v is 0.7 (close to the drifter value). The bottom figure is the same but with the average meridional velocity variance.

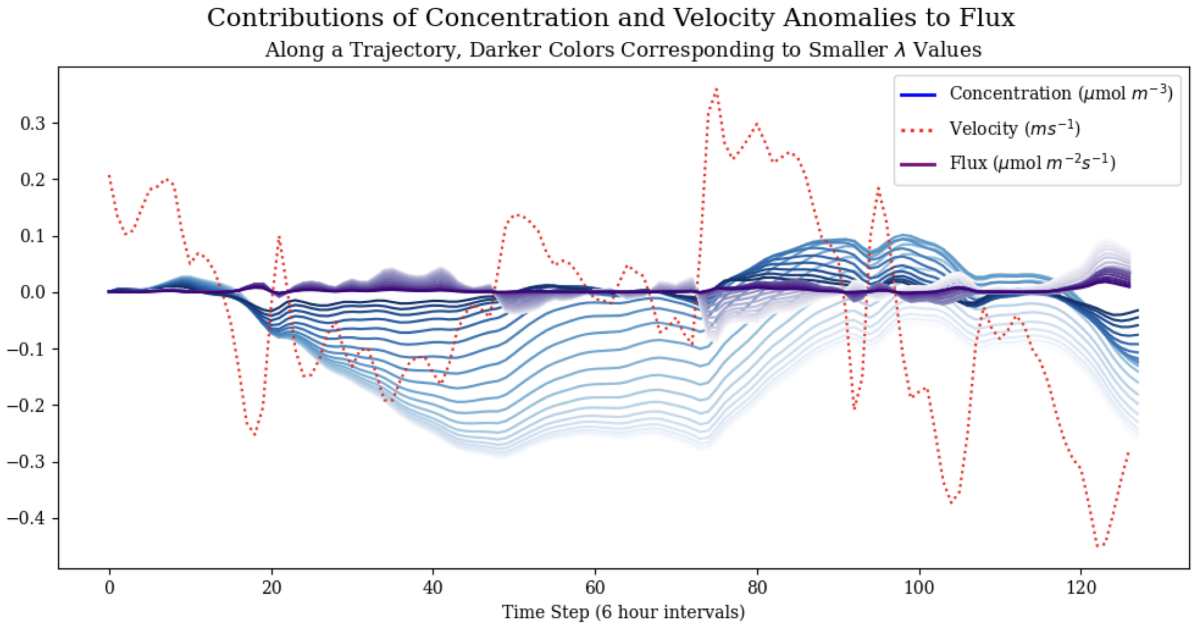

Figure S2: The contributions of the velocity and concentration anomalies, respectively, to the flux, for a randomly selected trajectory. Each blue and purple line corresponds to a different value of the uptake rate λ.

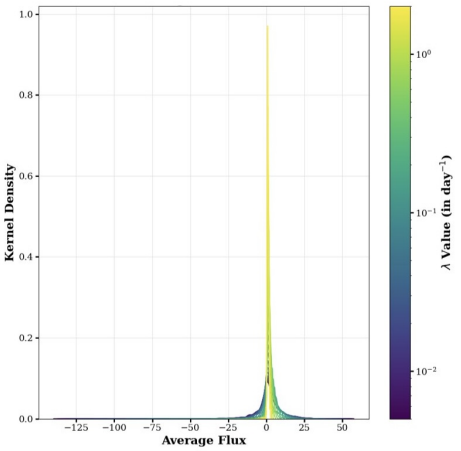

$\sigma_r^u = 0.100$, $\sigma_r^v = 0.450$, $\tau_r^u = 0.702$, $\tau_r^v = 0.691$

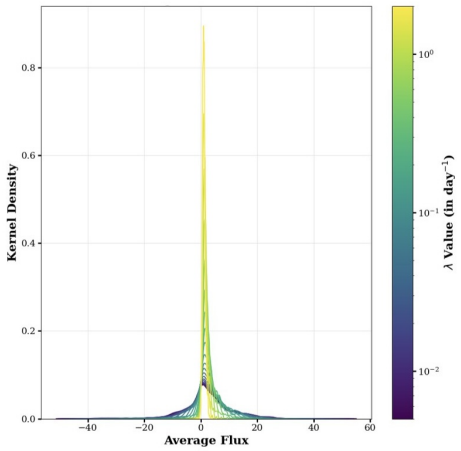

$\sigma_r^u = 0.175$, $\sigma_r^v = 0.15$, $\tau_r^u = 0.772$, $\tau_r^v = 0.698$

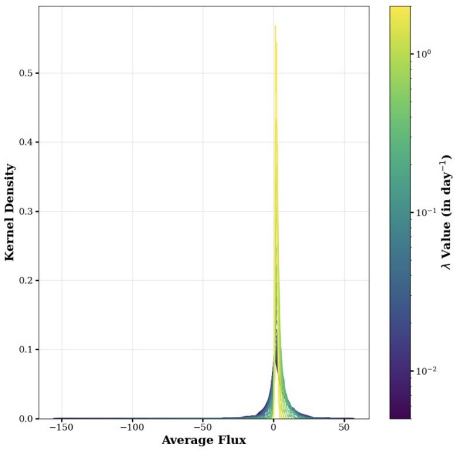

$\sigma_r^u = 0.218$, $\sigma_r^v = 0.271$, $\tau_r^u = 0.475$, $\tau_r^v = 1.025$

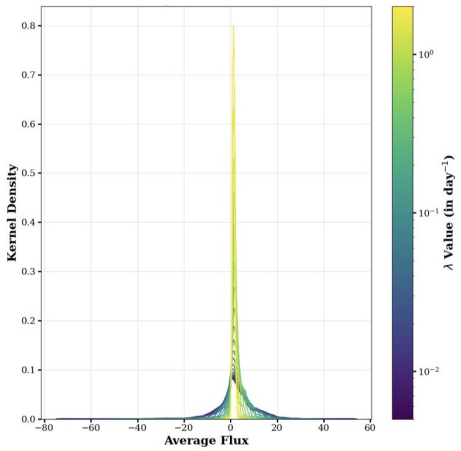

$\sigma_r^u = 0.218$, $\sigma_r^v = 0.271$, $\tau_r^u = 0.375$, $\tau_r^v = 0.25$

Figure S3: Distributions of the Lagrangian-averaged fluxes over the domain for four arbitrarily selected sample simulations. The top two have the calculated drifter values of τ whereas the bottom two have the calculated drifter values of σ. Each line within a plot is the flux computed for a different value of the uptake rate λ and is shaded accordingly. In each case, we see an approximate bell-curve, justifying the use of the domain average as a representative value.

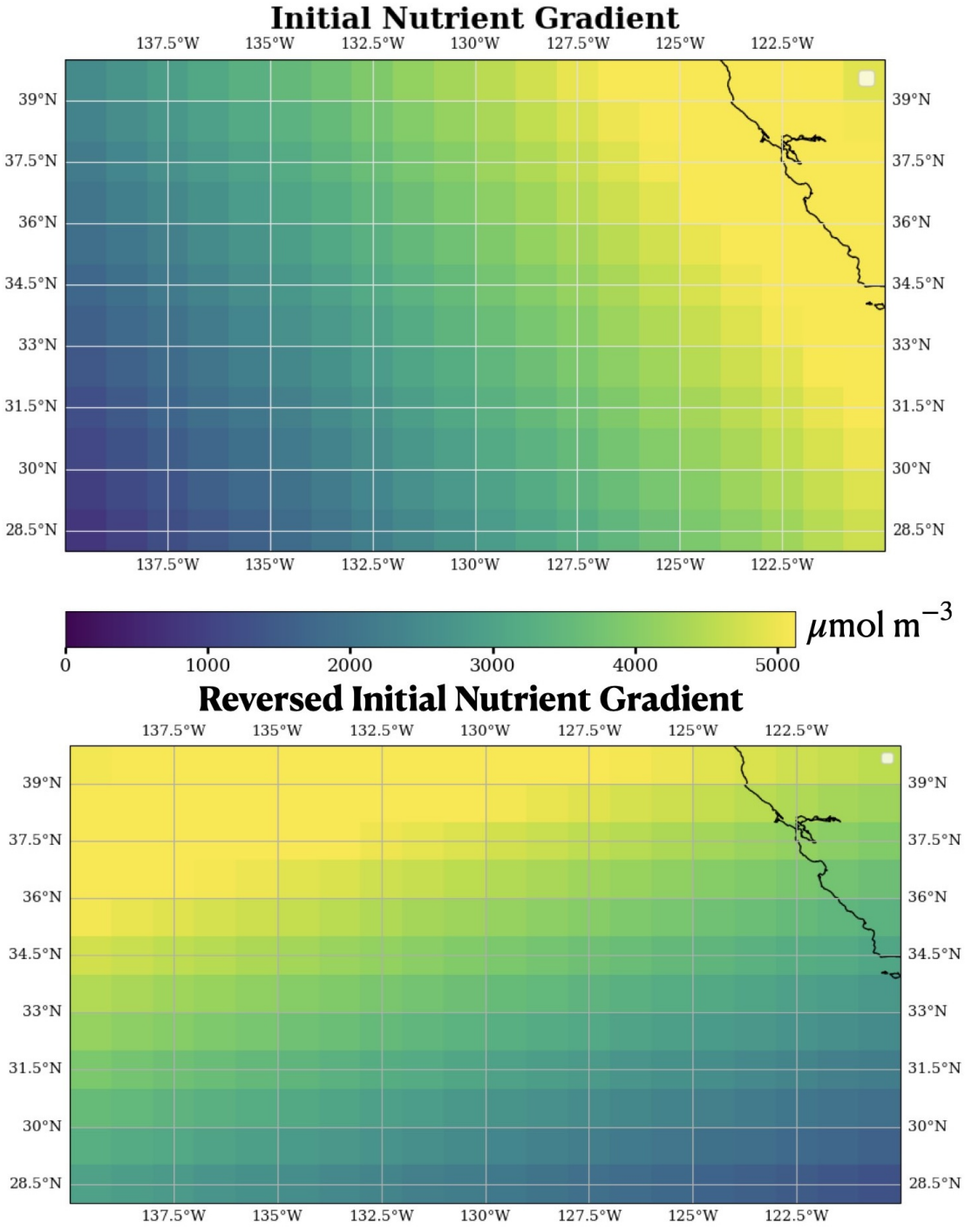

Figure S4: Comparison of the realistic background nutrient gradient, as in the main text (top), and reversed background nutrient gradient (bottom).

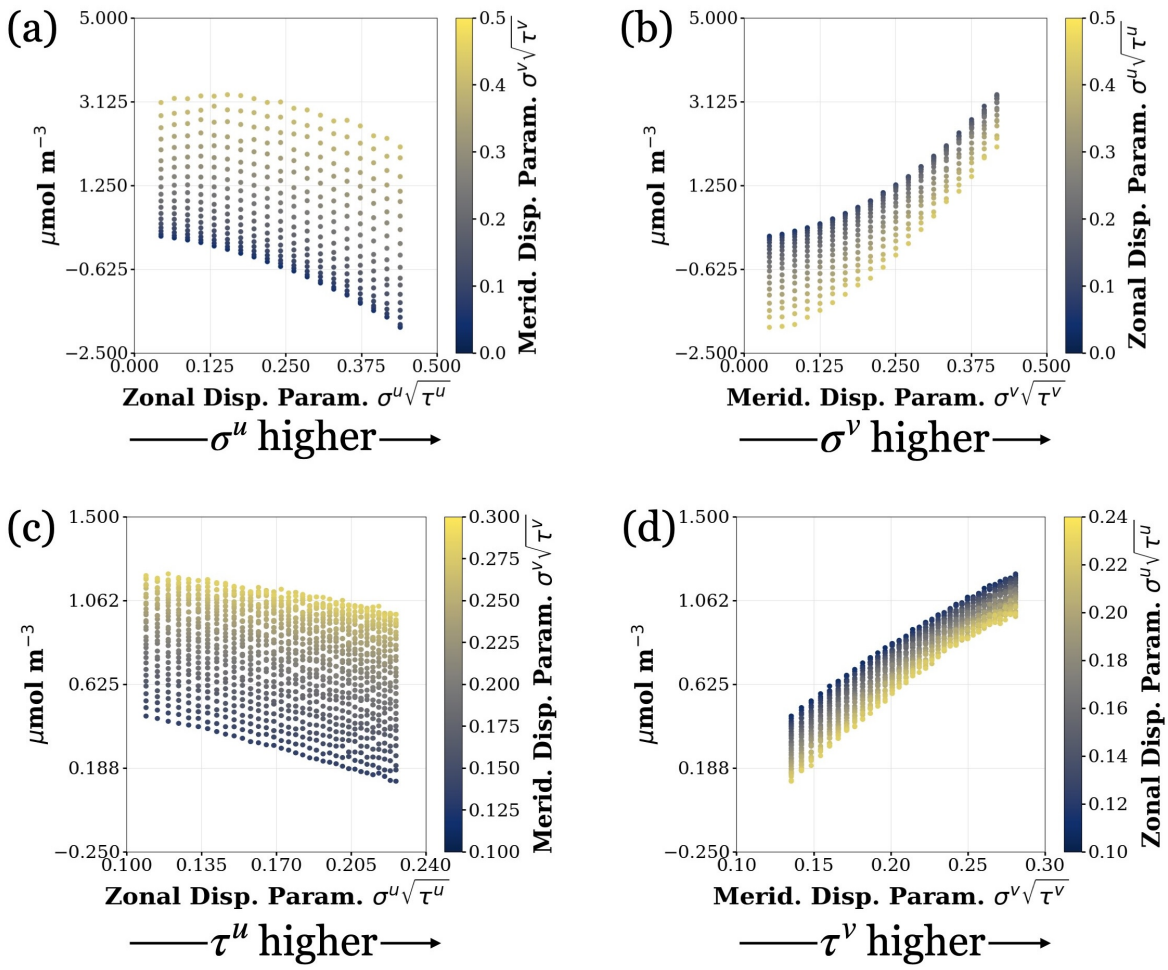

Figure S5: Figure 2 in the main text but for the reversed nutrient gradient. Top: The effect of varying the turbulent velocity fluctuations $\boldsymbol{\sigma}_r$ (a) zonally and (b) meridionally on the domain-averaged Lagrangian flux $\langle \boldsymbol{u}' P' \rangle_L$. The dispersion parameter in the relevant direction (e.g., zonally) is plotted on the x-axis, and the points are colored by the dispersion ratio in the other direction (e.g., meridionally). Each of these plots is for one, intermediate value of the uptake rate. Bottom: The same as the top panel, but illustrating the effect of varying the decorrelation timescale $\boldsymbol{\tau}_r$ (c) zonally and (d) meridionally on the average flux over Lagrangian trajectories. For each simulation, an intermediate uptake rate of $\lambda = 1.0645$ day^{-1} was used.

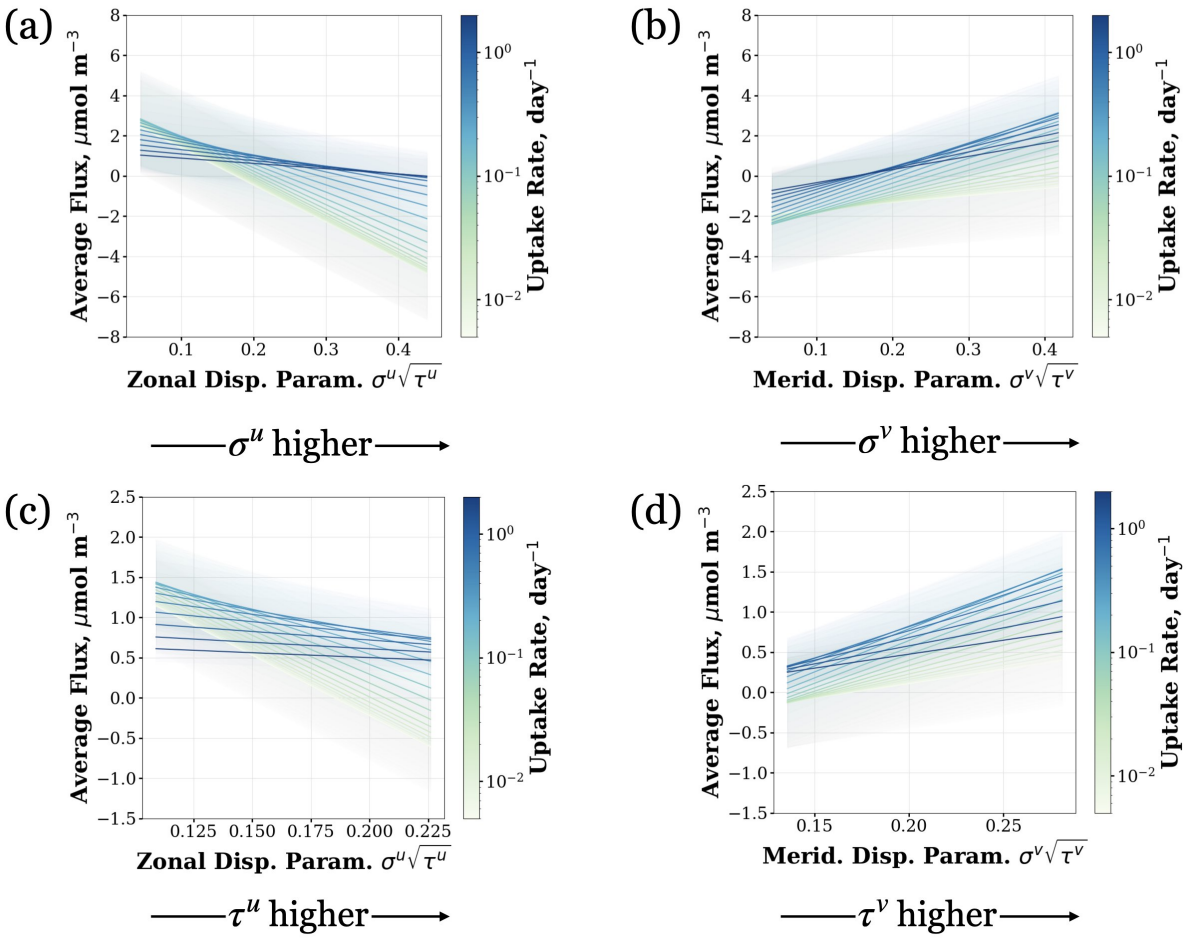

Figure S6: Figure 3 in the main text but for the reversed nutrient gradient. The best fit corresponding to a version of Figure S5 for each of the 20 uptake rates considered. Uptake rate is denoted by the line color. Shading shows the standard deviation. Top: the effect of varying the turbulent velocity fluctuations σ_r, (a) zonally and (b) meridionally. Bottom: the same as the top, but the effect of varying the decorrelation timescale τ_r, (c) zonally and (d) meridionally.

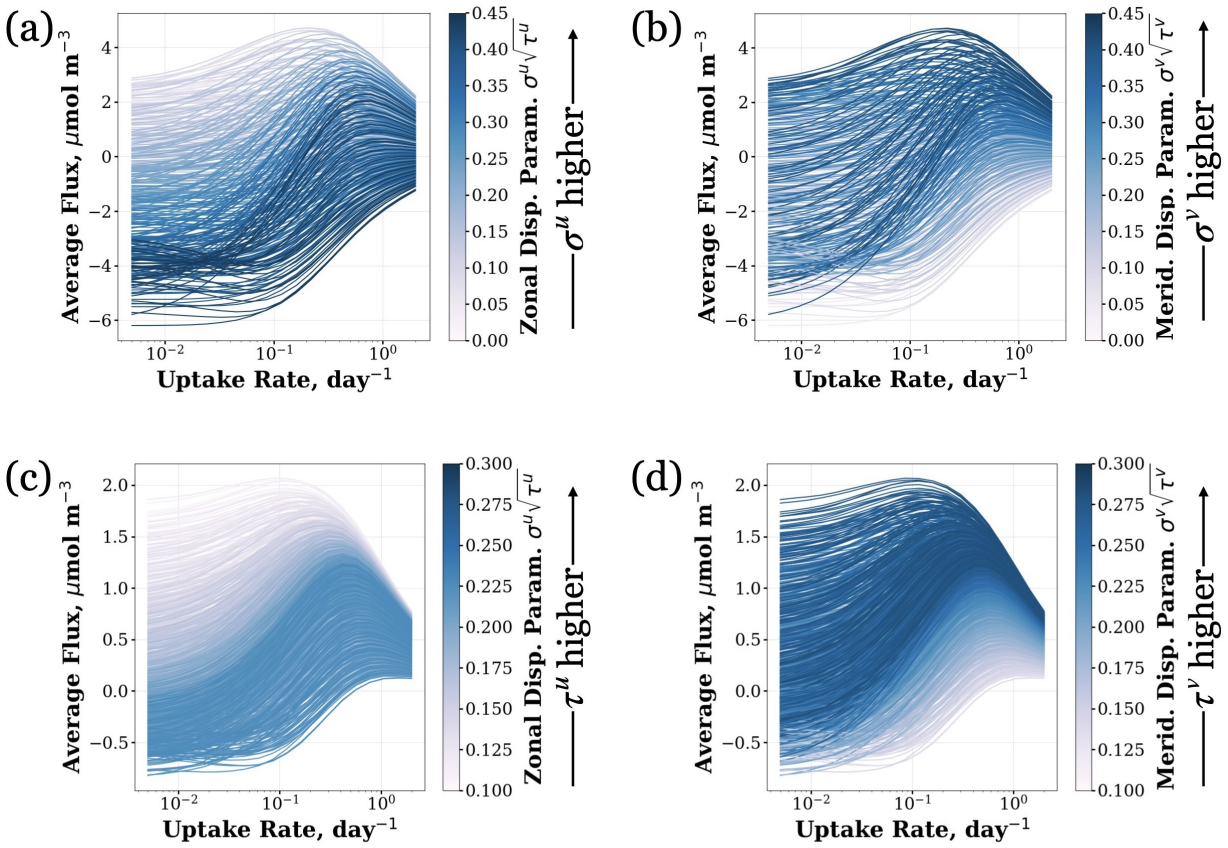

Figure S7: Figure 4 in the main text but for the reversed nutrient gradient. On the y-axis, the average flux across Lagrangian trajectories is plotted, with the uptake rate λ on the x-axis, for each different dispersion parameter value. Top: the relationship for different values of the dispersion parameter, where the dispersion parameter was increased by increasing the turbulent velocity fluctuations, (a) zonally (σ_r^u) and (b) meridionally (σ_r^v). Bottom: the same as the top, but where the dispersion parameter was increased by decreasing the decorrelation timescale, (c) zonally (τ_r^u) and (d) meridionally (τ_r^v).